# Photoinduced gel–liquid transition of DNA fluid generates remote-controlled nonequilibrium microflow

*Hirotake Udono*[1], *Shin-ichiro M. Nomura*[2], *Masahiro Takinoue*[1]*

1 Department of Computer Science, School of Computing, Tokyo Institute of Technology, Yokohama, Kanagawa, 226-8502, Japan.

2 Department of Robotics, Graduate School of Engineering, Tohoku University, Sendai, Miyagi, 980-8579, Japan.

*E-mail: takinoue@c.titech.ac.jp

# Abstract

We demonstrate remote-controlled microflow using photoinduced gel–liquid state transition of DNA fluid, which is micro-scale condensate of branched DNA nanostructures self-assembled through sticky end (SE) hybridization. The binding affinity of DNA nanostructures can be photoswitched by introducing azobenzene in SE, which leads to reversible gel–liquid state transition of DNA fluid. Assisted by DNA sequence programmability, we construct energy-transducing systems that convert photoinduced state transition to microflow of DNA fluid capable of mechanical manipulation. Azobenzene insertion sites in SEs determine specific flow modes, providing drastic mode switching between spreading, fetching, and gathering. Flow mobility is maximized at moderate temperatures in each flow mode. Thermodynamically, this anomalous "reentrant" flow-mobility behavior is explained as nonequilibrium microflow originating from enthalpy fine-tuning in SE binding affinity. These findings will contribute to emerging technologies for remote-controlled fluid manipulation within confined environment of biological/artificial cells, such as DNA-fueled transport, artificial micromuscles, and microstructure folding.

# Main body

## 1. Introduction

With the increasing sophistication of nano/micro technology, remotely controllable miniaturized objects have been the subject of interest in various research fields. Dynamic adjustment of structure[1,2], motion[3], and function[4] of micrometer-sized objects, such as microgels and liposomes, have been the primary focus. One disregarded target is the remote controllability of micrometer-sized fluid[5]. Notably, there has been an increasing demand for exploitable remote-controlled fluid for various mechanical manipulations due to an evolving interest in fluid manipulation within a confined environment such as micro-reactors[6], miniature soft robots[1,7], and artificial[8] or biological[5] cells. The potential examples include the deformation of soft microstructures[9] (*e.g.*, gels, droplets, membrane sheets[10], and even micro-wires[11]) and fluid-driven transport using diffusion and convection[5,12]. In the last few decades, microflow regulation has been investigated exclusively using microchannels that produce the fluid effects to achieve numerous tasks, such as solution mixing[13], droplet generation/manipulation[14], and particle sorting[15]. However, such top-down microfluidic approaches are unsuitable for microflow manipulation within a confined environment due to limited accessibility. Furthermore, active droplets capable of photocontrollable locomotion depend on the chemical interaction with a substrate that is interfaced with the droplets[16,17], preventing their introduction into biological/artificial cells. Consequently, the control mechanism and rational design for remote-controlled microflow are largely unknown.

Establishing remote-controlled microfluidic mechanical actions requires the following three mechanisms: (1) an energy-transducing mechanism, which receives and converts input energy to mechanical actions. This energy-transducing system should operate in an isothermal condition to

limit nonspecific chemical reactions within a confined environment. (2) An on/off switching capability which activates or deactivates the remote-controlled microflow upon a signal input. (3) The dynamics programmability based on encoded information. One instructive example of programmed dynamics is observed in liquid-like condensates, which arise through the liquid-liquid phase separation of biomolecules in living cells[18,19]. Membrane-free phase-separated liquid droplets, such as organelles[20] and nucleoli[21], form as a highly dynamic compartment due to specific molecular interactions of proteins and RNA with prescribed sequences. Living cells exploit this dynamic nature to maintain spatiotemporal coordination of biochemical processes[22,23], an autonomous organization of sub-compartmentalized structures[24], and fluidity change of phase-separated condensates through phase transition[23,25,26]. Therefore, the fluid property change is linked with many diseases, which develop from the dynamic molecular exchange malfunction[26].

For the programmable microfluidic dynamics, exploiting DNA as a design material is an appealing strategy[27] due to the high addressability and programmability in DNA binding sites[28]. The powerful molecular recognition capability of DNA has been exploited to control the self-assembly of highly structured nanosystems in the last few decades[28–31]. Beyond nanofeatures, the specific bonding mechanism of DNA has been used to form DNA hydrogels, which are a compelling target in numerous biomedical applications due to their high biocompatibility, easy synthesis, and functionalization[32,33]. Recently, DNA fluid, a micro-scale condensate of DNA nanostructures with well-engineered sequences that emerges through phase separation[34–40], has drawn significant attention due to their sequence-specifically directed interaction[34] and structural programmability[34,35,39]. Specifically, DNA fluid exhibits a temperature-dependent phase behavior between gel, liquid, and dispersed states, which is prescribed by sequential design[34,41]. However, DNA fluid still lacks the remote controllability of isothermal state transition and energy-

transducing mechanism, which are eagerly anticipated features for intracellular microfluidic control. To satisfy these requirements, photochemical reactions have distinct advantages as effective signal transmission, energy injection, and isothermal control, including minimal invasiveness and high-locality control[42–46]. In prior works, the photoregulated state transitions of DNA self-assembled matter have been achieved with low spatial locality due to high concentration threshold[47,48] or in low specificity because of photoswitchable surfactant usage[49].

In this study, we demonstrate remote-controlled microflow using photoresponsive DNA fluid. The DNA fluid was fabricated through the self-assembly of branched DNA motifs, nanostructures of base-paired single-stranded DNAs (ssDNAs): Three ssDNAs hybridized in the stem region to form a branched motif possessing sticky ends (SEs); via the hybridization of SEs, the branched DNA motifs self-assembled into DNA fluid, which was micrometer-scale condensates. The motifs were equipped with a photoresponsive capability by introducing azobenzene (Azo), well-studied photoisomerizable compound[44], in the SEs. The photoswitchable Azo isomerization enabled the reversible association/dissociation between branched DNA motifs, leading to photoreversible fluidity regulation via gel–liquid–dispersed state transition. To design an energy-transducing system, we exploited the following sequence-specific programmability of DNA. By cross-linking the photoresponsive DNA motif with a branched DNA motif possessing nonphotoresponsive orthogonal SEs, we achieved photocontrollable "transporter" DNA and "cargo" DNA fluids; the photoresponsive DNA fluid hydrodynamically performed mechanical actions upon the nonphotoresponsive DNA fluid by transducing light energy. Notably, we discovered multiple modes in the generated fluid's mechanical action as a function of the applied temperature and the Azo insertion site in the SE. Each flow mode was characterized as a single-peak-shaped profile in the temperature-dependent flow mobilities. The highest and lowest mobilities were obtainable in

moderate and lower and higher temperature ranges, respectively. This anomalous profile was analogous to the reentrant phase behavior of DNA microstructures[41,50,51], which behave as solid-like only in a moderate temperature range and as liquid-like in the lower and higher temperature ranges. Following thermodynamic arguments on the observed reentrancy, we describe the observed flow-mobility behavior as a manifestation of a transient non-equilibrium state in the SEs binding stability. We also explain the mode-changeability of the mechanical actions with experimental support by explaining the role of the Azo insertion site in the SE in determining the degree of the nonequilibrium in the binding stability.

## 2. Results and discussion

### 2.1 Photoresponsive DNA fluid

Fig. 1a describes the DNA fluid capable of photoresponsive state transition, which was enabled by introducing Azo, a photoisomerizable chemical compound, in nano-scale Y-shaped motifs of DNA (Y-motifs). The Y-motifs (Supplementary Table 1–4) had three-branched double-stranded stems that terminated in an overhang of a single-stranded SE with eight nucleotides (nt). The self-complementarity of the SEs provides the inter-motif connectivity that allows the nanoscale Y-motifs to self-assemble into a micro-scale DNA fluid. A prescribed annealing process caused a set of three single-stranded DNAs (ssDNAs) to self-assemble into a Y-motif through the stem hybridization, subsequently forming micro-scale fluid through the 8-base-pair (bp) SEs' duplex formation. One or two Azo residues were inserted in the SEs to provide the motifs with photoresponsive capabilities. Azo undergoes photoisomerization between the *cis* and *trans* isomers upon UV (300 nm $< \lambda <$ 400 nm) and visible light (Vis, $\lambda >$ 400 nm) irradiation, respectively. The *cis*-Azo destabilizes the base stacking of hybridized DNA strands and causes the hybridized strands to dissociate due to steric hindrance, whereas the *trans*-Azo strengthens the

duplex formation by stabilizing the base stacking[52]. Consequently, the Azo-modified DNA nanostructures can be reversibly dissociated/associated with each other in response to UV and Vis irradiation, respectively, due to the photoreversible *cis*/*trans* isomerization. Fig. 1b illustrates the photoswitching of SEs, which provides the principle mechanism for the photoregulated state transition of DNA fluid.

First, we demonstrate UV-induced gel-to-liquid state transition as in Fig. 1c. The sponge-like surface smoothed out, followed by increasing pore formation (Supplementary Movie 1) with UV (365 nm) irradiation upon a gel state of DNA fluids (see Supplementary Table 3 for its sequence design). Some gradually separated gels showed viscous threading and rounding-up (Fig. 1d). These morphological changes indicate an increase in the continuous shuffling of Y-motifs and thus a gel-to-liquid state transition. The liquefied DNA fluids dispersed after further UV exposure. Fig. 1e reveals the Vis-induced dispersed-to-liquid/gel transition. Initially, UV irradiation dissolved the DNA fluids, and upon switching to Vis (440 nm), punctate bodies' recondensations were captured (Supplementary Movie 2), indicating SE reassociation due to the Azo isomerizing into *trans*. Recondensation was observed only at high temperatures of approximately 60°C, indicating that frequent interactions between SEs due to substantial thermal fluctuations are essential for the recondensation. Compared to the bulk-scale state transition[47], the discrete condensed bodies within an irradiated area underwent the photoinduced state transition without affecting the bulk properties. Therefore, we verified that photoresponsive DNA can be used to modulate fluidity through reversible state transition.

In Fig. 2, we provide experimental support for the underlying mechanism of the reversible binding and unbinding of branched DNA nanostructures using native polyacrylamide gel electrophoresis (PAGE). In this study, we used Y-motifs with a single SE to form distinct binary

bands in a lane, each being equivalent to the associated (dimer) and dissociated (monomer) state of the single-SE motifs, respectively. As described in Fig. 2a, the single-SE motifs favor the formation of the monomer and dimer in response to UV and Vis, respectively. Fig. 2b shows the PAGE results as a function of irradiation wavelength and duration for the four types of DNA motifs that differed in the Azo insertion site. Throughout, we refer to Azo-containing SEs as $SE_{1x7}$, $SE_{3x5}$, and $SE_{2x1x5}$, respectively, where the subscript represents the Azo insertion site "x" in the 8-nt SE (Fig. 2b). For example, in $SE_{1x7}$, Azo residue divides the first 1 nt from the 5' end and the remaining 7 nts in the SE. In Fig. 2b, the upper (dimer) and lower (monomer) bands showed a decrease and an increase in the fluorescence intensity, respectively, with increasing UV irradiation; the upper and lower bands reverted to their original intensities upon subsequent 6-min Vis irradiation. Following the band intensities observed in Fig. 2c, we quantified the concentration of the binary states as a function of the irradiation to easily recognize the band intensity changes. The PAGE analysis verified the mechanism behind the photoreversible state transition, where the macroscopic state transition may be deterministically translated from the molecular-level photocontrolled binding and unbinding of DNA nanostructures.

We observed that the band intensity shift amplitude varied as a function of Azo insertion site in the SE (Fig. 2c): in the on/off photoswitching, $SE_{2x1x5}$ showed the most pronounced change, $SE_{3x5}$ a moderate shift; and $SE_{1x7}$ showed the lowest amplitude. This observation motivated us to investigate further the dependence of their photoresponsiveness on the insertion site of Azo in the SE.

2.2 Evaluation of SEs' binding strength

We measured the dissolving temperature $T_D$ based on the microscopic observation of DNA fluid to evaluate the binding strength of SEs. Fig. 3a. illustrates that DNA fluids dissolve and disappear

above $T_D$ with increasing temperature. $T_D$ serves as a measurable parameter for the thermostability of the SEs. Here, Y-motifs with three SEs as shown earlier in Fig. 1 were investigated. To measure $T_D$ for the *cis*/*trans* states, DNA fluids were exposed to UV/Vis irradiation and then heated on a thermoplate until complete dissolution into the buffer. Hereafter, Y-motif with each branch terminating in $SE_i$ ($i$ = 1x7, 3x5, 2x1x5) will be referred to $Y_i$ ($i$ = 1x7, 3x5, 2x1x5). As in Fig. 3b, we found that while $Y_{1x7}$-based DNA fluids showed the highest $T_D$, or the strongest binding stability, for both *cis*/*trans* among the photoresponsive SEs, followed by $Y_{3x5}$ and then $Y_{2x1x5}$. Furthermore, the *cis–trans* gap of $T_D$ showed an increase in this order. This agreed well with the observed increase in the amplitude of photoinduced concentration change of single-SE motifs as shown in Fig. 2c.

These results revealed that the location and number of Azo in the SE significantly affected the binding strength of the photoresponsive DNA motifs. An inward shift of Azo from 5' to 3' end in the SE (from $SE_{1x7}$ to $SE_{3x5}$) destabilized the binding strength, and an increase in the number (from $SE_{3x5}$ to $SE_{2x1x5}$) had a further destabilizing effect. At the molecular level, the bound and unbound states of SEs switch interchangeably from one state to the other in chemical equilibrium. In $Y_{3x5}$, where the two opposing Azo residues are closely located near the middle region of base-paired SEs, there is the possibility that the close residues may fall into *cis* coincidentally, leading to enhanced steric hindrance that disfavors the hybridized state. Similarly, in $Y_{2x1x5}$, two sets of Azos dominate the middle region of the hybridized SEs, causing additional instability in the SE binding. Conversely, in $Y_{1x7}$, the inserted Azo residues located near the terminal of the base-paired SEs are distanced apart from each other, thus causing a lesser possibility of the simultaneously enhanced steric hindrance.

2.3 Programmed mechanical actions using the microflow of DNA fluids

### 2.3.1 Multi-mode photogenerated hydrodynamics of DNA fluid

We designed DNA motifs combining Azo- and non-Azo-containing Y-motifs, aided by DNA sequence programmability, to create microflow-based mechanical actions. Different roles in the mechanical actions could be attributed sequence-specifically to two DNA fluids by combining the different phase behaviors of DNA fluids. One was the photoresponsive DNA fluid (Fig. 4a, green) containing $Y_i$ ($i$ = 1x7, 3x5, 2x1x5), and the other was a nonphotoresponsive DNA fluid (Fig. 4a, blue) comprising nonphotoresponsive Y-motif (referred to as $Y_0$) that was orthogonal to $Y_i$ in the SE sequence. Therefore, these DNA fluids in a liquid state do not coalesce due to their molecular recognition capability (Fig. 4a)[34]. However, by introducing six-branched cross-linker DNA $L_0$, three of whose six SEs selectively bonded with $Y_i$, and the other three with $Y_0$ (Fig. 4b)[34,39], these mutually immiscible DNA fluids were bound, resulting in the formation of an adhered structure of DNA fluids. Hereafter, the cross-linked DNA motifs forming the adhered DNA fluids will be referred to as $Y_i/L_0/Y_0$. A sequence-specific photoresponsive capability was realized in the adhered DNA fluids due to the introduction of Azo in the SEs of $Y_i$ (Fig. 4c, Supplementary Table 9). Fig. 4d shows the adhered DNA fluids in a gel state using fluorescence microscopy. The photoresponsive (green) and nonphotoresponsive (blue) DNA gel particles adhered well.

Due to the coexistence of sequence-specifically photoresponsive DNAs, energy-transducing systems (Fig. 5a) were formed, where the photoresponsive DNA fluid (Fig. 5a, green) received light as an energy source and on/off switching signal, and the photoinduced state transition could generate a microflow acting on the nonphotoresponsive DNA fluid (Fig. 5a, blue). Therefore, in this mechanical action, we designated “transporter” and “cargo” to the photoresponsive and nonphotoresponsive DNA fluids, respectively.

The photogenerated mechanical actions can be categorized into three modes based on the actions of the “transporter” DNA (green) exerted on “cargo” DNA (blue), as summarized in Fig. 5b.

The first mode is the "spread" mode (Fig. 5c), which was observed for $Y_{2x1x5}/L_0/Y_0$ motifs (< 40°C), $Y_{3x5}/L_0/Y_0$ (45°C–60°C), and $Y_{1x7}/L_0/Y_0$ (>60°). The "transporter" DNA dissolved rapidly into the buffer due to a fast gel-to-dispersed state transition upon UV (360–370 nm) irradiation, leading to an outward spread of the "cargo" DNA particles (Fig. 5d, Supplementary Movie 3).

Another mode is the "gather" mode (Fig. 5e), which was observed only for $Y_{1x7}/L_0/Y_0$ (35–50°C). The "transporter" DNA showed a gel-to-liquid state transition upon UV irradiation, and the subsequently emerging surface tension led to drastic compaction of the "cargo" DNA gel particles, which were sparsely scattered (Fig. 5f, Supplementary Movie 4). Notably, none of the "cargo" particles were left behind in the compacting motion because of the cross-linker adhesiveness.

The last mode is the "spread and fetch" mode (Fig. 5g), which was observed for $Y_{2x1x5}/L_0/Y_0$ (40°C–45°C) and $Y_{3x5}/L_0/Y_0$ (55–60°C). At the initial state, immiscible "transporter" and "cargo" DNA fluids constituted a sub-compartmentalized liquid droplet, where the "transporter" encompassed the "cargo." The "transporter" DNA favored the liquid-to-dispersed state transition upon UV irradiation, leading to a "spread" of the "cargo" DNA. Additionally, the diffused-out "transporter" DNA showed reversing flow due to dispersed-to-liquid state transition while dragging the "cargo" DNA droplets backward upon switching to Vis (520–550 nm) irradiation and finally, a sub-compartmentalized droplet was reformed (Fig. 5h, Supplementary Movie 5). Therefore, the observed reversing flow suggests that the Vis-induced reassociation of the SEs increased entropic elasticity, which served as an attractive force to reverse the flow and "fetch" the "cargo" DNA. The forward and reverse actions (Fig. 5g), which induced a muscle-like motion, could be repeated in approximately several cycles (Fig. 5i, Supplementary Movie 6, Supplementary Fig. 2). This limitation shows the imperfect photoswitching efficiency of the Azo molecule and the bulky geometry of the observation chamber used (For a more detailed discussion,

see Supplementary information[53–56]). The "spread and fetch" cycle was observed at temperatures ranges of 40°C–45°C ($Y_{2x1x5}/L_0/Y_0$) and 55°C–60°C ($Y_{3x5}/L_0/Y_0$), which were close to the dissolving temperature $T_D$ of its "transporter" DNA (*trans*, Fig. 3b), 50°C ($Y_{2x1x5}$) and 65°C ($Y_{3x5}$), respectively.

Fig. 5b shows the summary of the flow modes observed for each Azo insertion and their effective temperature ranges, in connection with the dissolving temperature $T_D$ from Fig. 3. With an increase in $T_D$, the effective temperature range of each flow mode increased to a higher range, and the "gather" mode was only available for the lowest *cis–trans* $T_D$ gap in $Y_{1x7}/L_0/Y_0$.

### 2.3.2 Reentrant temperature dependence of flow mobility

The mobility of the produced microflow in each abovementioned flow mode exhibited the greatest mobility in a moderate temperature range but slowed down in the lower and higher temperature ranges ("spread" mode of $Y_{2x1x5}/L_0/Y_0$, Fig. 6a; "gather" mode of $Y_{1x7}/L_0/Y_0$, Fig. 6b). To quantitatively analyze this anomalous temperature-dependent flow mobility, we derived the mean square displacement (MSD) of the "cargo" ($Y_0$) particles in the observed trajectories in $Y_i/L_0/Y_0$ ($i$ = 1x7, 3x5, 2x1x5). A range of temperatures from room temperature (RT) to 60°C ($i$ = 1x7, 3x5) or 45°C ($i$ = 2x1x5) was investigated. The resultant trajectories of the "cargo" particles were subjected to particle tracking analysis using TrackMate[57], an open-source Fiji plugin (Supplementary Fig. 3), and subsequent conversion to MSD plotting. We provide representative MSDs as a function of time interval $\tau$ for the "spread" mode of $Y_{2x1x5}/L_0/Y_0$ (Fig. 6c) and the "gather" mode of $Y_{1x7}/L_0/Y_0$ (Fig. 6d) from low, middle, and high temperature ranges. We confirmed that the MSD curves showed marked upward curvature in the middle temperature ranges, compared to those in the lower and higher temperature ranges. The marked upward curves

in the middle temperature range indicate the ballistic nature of the photogenerated migrations rather than the random Brownian motion, which normally displays the linear slope in the MSD curve (Supplementary information)[58,59].

For a comprehensive evaluation of the flow mobility at various temperatures, we further calculated the diffusion coefficient $D'$ of individual trajectories of the "cargo" particles from a linear curve fitting against their MSD curves (Supplementary eq.2). To consider the direction of the generated migrations, we arbitrarily defined a signed diffusion coefficient $D^*$, where $D^* = -D'$ in the case of inward-directed flow, as observed in the "gather" mode and the reverse phase of the "spread and fetch" mode, and $D^* = D'$ otherwise (Fig. 6e). The signed $D^*$ was plotted as a function of $T$ for alternating UV and Vis irradiation (Fig. 6f).

We found distinct single-peak profiles for the "spread" mode ($Y_{2x1x5}/L_0/Y_0$ and $Y_{3x5}/L_0/Y_0$), the "gather" mode ($Y_{1x7}/L_0/Y_0$) for UV (Fig. 6f), and the reverse phase of the "release and fetch" modes ($Y_{2x1x5}/L_0/Y_0$ and $Y_{3x5}/L_0/Y_0$), as shown earlier in Fig. 6a–d. Interestingly, we found a marked peak shift by 20°C between $Y_{3x5}/L_0/Y_0$ and $Y_{2x1x5}/L_0/Y_0$ and a drastic peak inversion between $Y_{3x5}/L_0/Y_0$ and $Y_{1x7}/L_0/Y_0$. These drastic $D^*$ profile changes show that the microflow of DNA fluid can undergo a drastic mode switch via minor molecular-level relocation of Azo residues in the SE without re-designing the motif sequences. On a closer inspection, $Y_{1x7}/L_0/Y_0$ showed a negative-to-positive sign inversion, which was a mode shift from the "gather" to "spread" modes, close to 60°C.

The single-peak profiles of $D^*$ for the photoinduced mechanical actions were observed in this study. We call these profiles as a "reentrant flow-mobility behavior." It was inspired by the previously reported reentrant melting behavior of DNA star-shaped nanostructures[41] and DNA-grafted micro-particles[50,51]. In the temperature-dependent phase diagram, at very high and low

temperatures, the DNA microstructures of interest favor a fluid phase, and at moderate temperatures, they equilibrate in a solid phase. The "reentrant melting behavior" appears in a system with two coexistent but competing DNA hybridization mechanisms toward the macroscopic state transition[41,50,51]. Thus, our reentrant flow-mobility behavior should have a different mechanism from the reentrant melting behavior. We attribute this mechanism to enthalpy difference in the SE hybridization of photoresponsive DNA motifs, which would change in response to UV or Vis light exposure. This photoinduced enthalpy shift in the SE hybridization would provide the underlying mechanism of the reentrant flow-mobility behavior (Fig. 7a).

We introduce a phase diagram that spans the $|\Delta H|$–$T$ space to understand the thermodynamics of the observed reentrancy of flow mobility (Fig. 7b). Here, $\Delta H$ indicates the difference between the enthalpy of the bound state of SEs and that of the unbound state of the SEs at equilibrium, as illustrated in Fig. 7a; that is, $|\Delta H|$ corresponds to the binding strength of the SEs. For photoresponsive DNA fluid, the bound–unbound enthalpy difference depends significantly on the isomeric state of Azo residues introduced in the SEs: *trans*-Azo and *cis*-Azo enhance the stacking and unstacking of the SEs, respectively, providing a photoswitching mechanism in the bound/unbound enthalpy difference[27,60]. UV irradiation promotes the *trans*-to-*cis* isomerization and a dynamic increase in $\Delta H$ by the amount of $\Delta(\Delta H)_{trans\rightarrow cis}$[60,61], whereas Vis causes a *cis*-to-*trans* isomerization accompanied by $-\Delta(\Delta H)_{trans\rightarrow cis}$. Therefore, the photocontrolled SE switching can be described as an isomerization-guided pathway in the $|\Delta H|$–$T$ phase diagram, which is in the form of a downward and upward vertical shift, as illustrated in Fig. 7b. The isomerization pathway causes no change in the phase properties in a very low temperature range (L) since the gel–liquid phase boundary is distant. Similarly, no significant change at very high temperatures (H) is observed in the isomerization since the path is below the liquid–dispersed

boundary. However, the isomerization pathway can cross the boundary only within the intermediate temperature window (M), which leads to a significant fluid effect via the macroscopic phase transition. The inclusion of the photocontrollability over the SE binding, in addition to the thermal control, produce two conflicting mechanisms of heat vs. light toward the SEs' binding. This competition allows access to the strong mechanical action within a period of moderate temperature.

Furthermore, the observed horizontal shift (between $Y_{3x5}/L_0/Y_0$ and $Y_{2x1x5}/L_0/Y_0$) and drastic sign inversion (between $Y_{3x5}/L_0/Y_0$ and $Y_{1x7}/L_0/Y_0$) of the $D^*$ profiles, as shown in Fig. 6f, can be explained by the vertical length of the isomerization path within the intermediate temperature window. Based on the discussion above, the vertical length of the path corresponds to a photogenerated difference in the SEs' binding enthalpy between the two isomers $|\Delta(\Delta H)_{trans\rightarrow cis}|$ (Fig. 6a). The dissolving temperature $T_D$ as measured in Fig. 3 indicates the binding strength of the SEs, and thus serves as a measurable parameter of $|\Delta H|$. As shown in Fig. 3b, the *cis–trans* $T_D$ gap depended on the insertion site of Azo residues in the SE. These considerations suggest that the Azo insertion site in the SE defines a reaction pathway, corresponding to $|\Delta H|$, in the $|\Delta H|$–$T$ phase diagram. For $Y_{1x7}/L_0/Y_0$ with $SE_{1x7}$ undergoing the lowest $T_D$ gap and thus the lowest $|\Delta(\Delta H)_{trans\rightarrow cis}|$, the *trans*-to-*cis* isomerization path crossed the gel-to-liquid phase boundary but not as far as the liquid-to-dispersed phase boundary. This moderate photogenerated $|\Delta(\Delta H)_{trans\rightarrow cis}|$ produced the pronounced fluid effect, *i.e.,* the surface tension-mediated large compaction of the "cargo" ($Y_0$) gel particles, as shown in Fig. 5f. In contrast, for $Y_{3x5}/L_0/Y_0$ and $Y_{2x1x5}/L_0/Y_0$ with a significantly larger $|\Delta(\Delta H)_{trans\rightarrow cis}|$, the isomerization paths were long enough to cross the liquid–dispersed boundary, and favored a gel-to-dispersed state transition, which was a driving force for the "spread" mode (Fig. 5d). This led to a drastic sign inversion of $D^*$ from

$Y_{1x7}/L_0/Y_0$. Furthermore, compared to $Y_{3x5}/L_0/Y_0$, Fig. 3b suggests that $Y_{2x1x5}/L_0/Y_0$ with a much wider *cis–trans* $T_D$ gap in $SE_{2x1x5}$ possessed a higher $|\Delta(\Delta H)_{trans\rightarrow cis}|$. Hence, $Y_{2x1x5}/L_0/Y_0$ extended its pathway further downward, and caused a marked downshift of the temperature window for the pronounced gel-to-dispersed phase transition.

In this study, we demonstrated that even minor relocation (2-bp shift and 2× increase) of Azo residues in the SE at the molecular level can deterministically translate to a drastic flow-mode switch. Thus, when compared with other molecular combinations, our method to combine DNA sequence programmability with Azo-based enthalpy fine-tuning could be an exceptional technique for versatile, simple microflow manipulations with mode switchability for the following two reasons: firstly, the effective fluid manipulation only requires a two-step prescription at DNA motif design and Azo insertion site in the SEs. The second law of thermodynamics determines that it is not trivial to ensure fluid reconstruction[62] and remodeling[63] while paying for the huge entropic cost of the macroscopic aggregation[27,41]. Therefore, this demanding task can be solved due to its programmable molecular selectivity and affinity between matched strands[41]. Without engineering the hybridization enthalpy in the SE sequence design, the Vis-driven reversing flow, as shown in Fig. 5h, would be unachievable since the Vis-induced duplex reformation of the SEs must compensate for the huge entropic cost accrued by a massive reduction of the freely dispersed motifs. To realize a specific hydrodynamic manipulation, the first step is thus to define the baseline of the SEs' binding affinity $|\Delta H|$ to specify the phase property in the initial state[34]; and the second is by prescribing the photodynamically-tunable enthalpy gap between *cis*-Azo and *trans*-Azo isomers $|\Delta(\Delta H)_{trans\rightarrow cis}|$. A specific flow mode and its "hot spot" temperature range for the effective manipulation will be favored as a result of this two-step design in Azo-modified DNA sequences. Secondly, the sequence programmability of DNA is remarkably useful in designating

specific roles, "transporter" and "cargo," to different DNAs. The sequence-specific photoresponsive systems allow different phase behaviors to be coupled in a purely DNA-based chassis, as shown in Fig. 5a. The use of other photoreactive molecules could not offer such a facile method for coupling multiple phase behaviors, and hence annoy researchers and engineers due to the cumbersome manufacturing processes. Note that for the purpose of demonstrating the sequence specificity, we chose DNA as "cargo," but other biomolecules or micro-beads could play a similar role, although with a lower degree of programmability in flow dynamics.

## 3. Conclusions

We demonstrated a remote-controlled microflow of DNA fluid using photocontrollable hybridization enthalpy between DNA motifs of well-engineered sequences. We endowed the DNA fluid with photoresponsiveness by introducing Azo resides in the SEs as the on/off signal transmission and energy injection mechanism. The DNA fluid demonstrated highly localized controllability over their macroscopic state transition between the gel, liquid, and dispersed states in a wavelength-dependent manner. The native PAGE analysis strongly supported the photoswitchable binding/unbinding mechanism underlying the macroscopic state transition. Simple molecular-level relocation of Azo residues in the SE significantly changed the dissolving temperature $T_D$, which is a measure of the SEs' binding enthalpy $\Delta H$, without time-consuming motif re-designing. The clear dependence of the *cis–trans* $T_D$ gap on the Azo insertion site in the SE suggests the ability of the inserted Azo to fine-tune the SEs' binding strength. Additionally, we demonstrated three modes of photogenerated mechanical actions of the sequence-specific photoresponsive DNA systems, coupling photoresponsive and nonresponsive motifs by a branched cross-linker. The photoinduced microflow showed reentrant-shaped temperature dependence due to the additional photoswitching mechanism competing with the thermal control toward the phase

behavior. Furthermore, we revealed that a molecular-level minor repositioning of Azo residues in the SEs favored a dynamic shift of the bound/unbound enthalpy difference in the SEs' hybridization; the resulting transient nonequilibrium microflow executed the mechanical actions. Therefore, this phototunable enthalpy control prescribes a specific flow mode with a distinct "hot spot" temperature window for effective fluid manipulation.

The simplicity and versatility demonstrated in our proposed DNA-based fluid regulation can be widely applied within a confined biological/biomimetic environment that is inaccessible with conventional top-down microfluidics methods. Notably, our method only requires sequence programming and simple fine-tuning of the photoreactive agents in the SEs. Therefore, this advantageous feature of our method would provide a facile, versatile mechanistic tool for micro-scale fluid manipulation. The "spread" mode could provide a novel technique for DNA-fueled transport. Our method does not rely on the complex use of multiple chemical compounds and time-consuming manufacturing processes compared to the Janus particles extensively studied so far[58,64]. The "gather" mode may also experience widespread application in artificial cell-like systems for dynamic compaction of their large substructures composed of biomolecules. The reversible "spread and fetch" mode may facilitate an on-the-spot controlled release of biomolecules from an agent-carrying cargo in drug manufacturing processes. Furthermore, the "spread and fetch" cycling might be applied as an actuation mechanism for artificial muscles in soft robotics. On a microfluidic platform, the "spread and fetch" cycling may also function as a remote-controlled micropump that regulates molecular transport within a confined environment.

# Materials and Methods

1. DNA motif construction

**Sequences** The photoresponsive Y-motifs and the cross-linked DNA systems were designed using the oligonucleotides listed in Supplementary Tables 1–9. The basic sequence designs were referenced from a previous study[34]. The DNA motifs were equipped with photoresponsive capabilities by introducing Azo into the SEs.

We purchased Azo-modified oligonucleotides from Tsukuba Oligo Service (Ibaraki, Japan), and the other non-Azo-modified strands were purchased from Eurofins Genomics (Tokyo, Japan). The former sequences were purified with high-performance liquid chromatography, and the latter sequences were purified with an oligonucleotide purification cartridge (OPC). The oligonucleotides were dissolved in ultrapure water (Milli-Q, 18.2 MΩ cm, Direct-Q UV 3 with Pump, Merck KGaA, Darmstadt, Germany) at a concentration of 100 $\mu$M upon arrival at the laboratory and stored in a –30℃ freezer until use.

**Material composition** In Y-motifs (Supplementary Tables 1–4), an equimolar mixture of three ssDNAs to jointly form Y motifs was dissolved in a test tube at a final concentration of 5.0 $\mu$M in a buffer containing 350 mM NaCl (> 99.5% purity, FUJIFILM Wako Pure Chemical Corp.) and 20 mM Tris-HCl pH 8.0 (UltraPure, Thermo Fisher Scientific, MA, US). For confocal microscopy, fluorescent dye (SYBR Gold Nucleic Acid Gel Stain, Thermo Fisher Scientific) was added to the buffer at a 1× concentration.

In cross-linked DNA systems (Supplementary Table 9), a mixture of Azo-containing ssDNAs (15 $\mu$M $Y_i$-1, 13.5 $\mu$M $Y_i$-2, and 15 $\mu$M $Y_i$-3) with 1.5 $\mu$M $Y_i$-2_FAM and non-Azo-containing ssDNAs (5 $\mu$M $Y_0$-1, 4.5 $\mu$M $Y_0$-2, and 5 $\mu$M $Y_0$-3) with 0.4 $\mu$M $Y_0$-2_Alexa405 and

0.1 $\mu$M $Y_0$-2_Cy3 to jointly form a sequence-specifically photoresponsive DNA motif was dissolved in the same buffer similar to that of Y-motifs. A 10% fraction of $Y_i$-2 and $Y_0$-2 were the dye-labeled strands. The concentration ratio of $Y_0$-2_Alexa405 and $Y_0$-2_Cy3 was 4:1 to strengthen the detectability of Alexa405, whose effective excitation wavelength deviated from that of UV irradiation applied. Note that $i$ = 1x7, 3x5, 2x1x5.

**Annealing protocol** For Y-motifs, DNA-dissolved solutions were heated from RT up to 85°C with a ramp of +1.0°C/min, held for 3.0 min, and cooled down to 25.0°C with −1.0°C/min.

For cross-linked DNA systems, DNA-dissolved solutions were heated from RT up to 85°C with a ramp of +1.0°C/min, held for 3.0 min, cooled down to 64.0°C with −1.0°C/min, held for 30 min, cooled down to 56°C with -0.25°C/min, and quickly cooled down to 25.0°C with −2.0°C/min.

These protocols were programmed and executed on a thermal cycler (Mastercycler Nexus X2, Eppendorf, Hamburg, Germany).

2. Microscopy observation

**Observation chambers** For Y-motifs, a 30-mm × 40-mm No.1 glass plate (thickness 0.13–0.17 mm, Matsunami Glass Ind., Ltd., Kishiwada, Japan) was treated with BSA (bovine serum albumin, FUJIFILM Wako Pure Chemical Corp.) coating. First, the glass was soaked and shaken for > 15 min in a BSA-containing solution (5 w/v% BSA and 20 mM Tris-HCl). As a spacer, a 20-mm × 20 mm square piece was cut from a silicone rubber sheet (1 mm × 300 mm × 300 mm, Tigers Polymer Co., Ltd., Osaka, Japan), and a 5-mm-diameter hole was pierced into it. Next, after the spacer was affixed to the glass plate, a 4-$\mu$L sample was applied within the pierced hole, which was then filled with mineral oil (Nacalai Tesque, Inc., Kyoto, Japan) to avoid dehydrating the sample.

For cross-linked DNA systems, samples were confined tightly between glass plates to minimize unwanted flow disturbance. A 2.5-$\mu$L sample was sandwiched between a BSA-treated 30-mm × 40 mm No.1 glass plate and an 18-mm x 18 mm No.1 cover glass (Matsunami) spaced by double-sided tape. Subsequently, the resultant confined space was filled with mineral oil through capillary sucking. Finally, the opening slits between the plates were sealed using a top coat.

**Temperature control** For Y-motifs, during the confocal microscopy observation, the sample-harboring pierced-hole chamber was placed on a Peltier heating stage (10021-PE120, Linkam Scientific Instruments Ltd., Surrey, UK).

For cross-linked DNA systems, during the fluorescence microscopy observation, the sample-sandwiching chamber was placed on a thermoplate (TPi-110RX, Tokai Hit Co., Ltd., Fujinomiya, Japan).

**Imaging** In Fig. 1 and Fig. 4, the samples were visualized using a confocal laser scanning microscope (FV1000, Olympus, Tokyo, Japan). For imaging of Y-motifs (Fig. 1), a 10× objective (UPlanSApo, Olympus) was used; for snapshots of cross-linked DNA systems at the initial state (Fig. 4), a 50× long-working-distance objective (LMPLFLN, Olympus) was employed.

In Fig. 3, Fig. 5, Fig. 6, and Supplementary Fig. 2, for fluorescence and phase-contrast (PC) imaging, a fluorescence microscope (IX71, Olympus) was used for $T_D$ evaluation of the photoresponsive Y-motifs (Fig. 3) and for capturing the photoinduced flow dynamics of the cross-linked DNA systems (Fig. 5, Fig. 6, and Supplementary Fig. 2) with a 60× objective lens (LUCPlanFL N, Olympus) in place. A bright-field filter was mounted for PC imaging. Finally, the images acquired were merged and adjusted using ImageJ.

3. Native PAGE

**Single-SE Y-motifs** In the control experiments, single-SE DNA motifs without Azo were used (Supplementary Table 5); photoresponsive single-SE DNA motifs with $SE_i$ ($i$ = 1x7, 3x5, 2x1x5) were considered for the irradiation effects on SEs' photoswitchability (Supplementary Tables 6–8). The annealing process and buffer condition of the single-SE motifs were identical to those of triple-SE Y-motifs.

**Gel electrophoresis** A mixture of 2.5-mL 40 w/v%-Acrylamide/Bis Partitioned Solution (29:1, Nakalai Tesque) and 2.0-mL 5× TBE (Tris-borate EDTA Buffer, Nippon Gene, Toyama, Japan) was topped up to 10 mL with Milli-Q in a test tube to prepare an 8-cm × 8-cm gel plate with 10% concentration. Subsequently, the tube was gently inverted several times after adding 150 $\mu$L of 10 w/v% APS (ammonium persulfate, FUJIFILM Wako Pure Chemical Corp.). After adding 3.0-$\mu$L TEMED (N, N, N', N'- tetramethylethylenediamine, FUJIFILM Wako Pure Chemical Corp.), the tube was inverted similarly. The solution was incubated for 60 min in an assembled gel electrophoresis cassette for polymerization.

For each lane in "Control," "$SE_{1x7}$," "$SE_{3x5}$," and "$SE_{2x1x5}$" (Fig. 2), an equimolar 1.0-$\mu$L mixture of the photoirradiated sample and 2× loading buffer was loaded within a designated well in a 4°C room. 100-bp ladder (Quick-load, New England Biolabs, Ipswich, MA, US) was loaded at 0.8 $\mu$L in the rightmost lane. The 2× loading buffer contained 1.0 w/v% BPB (bromophenol blue, FUJIFILM Wako Pure Chemical Corp.), 10 v/v% glycerol (FUJIFILM Wako Pure Chemical Corp.), and 50-mM EDTA (ethylenediaminetetraacetic acid, FUJIFILM Wako Pure Chemical Corp.). Next, gel electrophoresis was conducted in the 4°C room with a PowerPac Basic Power Supply (Bio-Rad Laboratories, CA, US) for 80 min at a constant voltage of 40 V. Finally, for fluorescence staining, the gel plate was soaked and gently shaken at RT for 5 min in 100-mL 1×

TBE containing 0.01 v/v% SYBR Gold. Finally, the gel plate was imaged with a Gel Doc EZ (Bio-Rad Laboratories).

**Quantification of the bands** The images acquired of the gel plates were subjected to quantitative analysis for the staining intensity using ImageJ. Within a selection rectangle covering a stained band, the "Integrated Density" ("IntDen") command was executed to consider the concentration of the corresponding motif state (monomer or dimer).

4. Light irradiation

In Fig. 1 and Fig. 3, a xenon lamp (300 W, MAX-303, Asahi Spectra, Tokyo, Japan) was used as a light source for photoswitching DNA self-assemblies. Light intensity was measured using a power meter (3664, Hioki E. E. Corp., Ueda, Japan) connected with a lightweight sensor (9742, Hioki E. E. Corp.). The light intensities used were 0.34 mW for $\lambda_{ex}$ of 365 nm ("UV," Fig. 1c) and 7.9 mW for 440 nm ("Vis," Fig. 1e).

In Fig. 2, for the irradiation of samples to load in the PAGE experiments, they were encapsulated in glass capillaries (ID: 1.12 mm, OD: 2 mm; World Precision Instrument, FL, US) because of their high UV transmittance and ease of handling a minute amount of liquid (Supplementary Fig. 1). The glass capillaries were irradiated while being placed on a black metal plate to avoid the visible light reflection of UV light from the surface. The light intensities irradiated were 2.7 mW ("UV") and 7.6 mW ("Vis").

In Fig. 3, Fig. 5, Fig. 6, and Supplementary Fig. 2, we observed the photogenerated migrations of the cross-linked DNA systems using the IX71. We set the excitation filter to $\lambda_{ex}$ of 360–370 nm ("UV," 3.3 mW) for the *trans*-to-*cis* isomerization of Azo in the photoresponsive Y-motif $Y_i$ and the excitation of Alexa405 introduced in the nonphotoresponsive Y-motif $Y_0$. For the excitation of FAM in $Y_i$ to capture the initial states of the samples, the excitation filter was set to

460–495 nm (7.0 mW). Additionally, the filter was set to 520–550 nm ("Vis," 4.8 mW) for the *cis*-to-*trans* isomerization of Azo in $Y_i$ and the excitation of Cy3 introduced in $Y_0$.

5. Measurement of the dissolving temperature $T_D$

Before the experiments in Fig. 3, we irradiated the samples with Vis light and observed $T_D$ for *cis*/*trans* Azo isomers while exposing them to UV/Vis. Different combinations of microscopes and heating stages were used as follows: (1) the confocal microscopy (FV1000) and the Peltier heating stage for the samples whose $T_D$ were apparently greater than 60°C; and (2) the fluorescence microscope (IX71) and the thermoplate (Tokai Hit). The thermoplate was carefully calibrated using its auxiliary temperature sensor.

We observed "Control," "$SE_{1x7}$ (*trans*)," and "$SE_{3x5}$ (*trans*)" using the combination of (1) the FV1000 and the Peltier heating stage. After attaining a given temperature and a subsequent 5 min incubation, we examined whether DNA fluids were dispersed in the buffer while scanning the sample with the 488-nm laser. When the DNA fluids were invisible, the temperature was determined to be $T_D$ for the sample of interest. Otherwise, the applied temperature was increased by approximately 1°C, and the same procedure was repeated until complete dissolution was detected. For $T_D$ < 60°C, we observed "$SE_{1x7}$ (*cis*)," "$SE_{3x5}$ (*cis*)," and "$SE_{2x1x5}$ (*cis*/*trans*)" using the combination of (2) the IX71 and the thermoplate. The samples were examined using PC microscopy with the background illuminated as weakly as possible to minimize the Vis effect from the bright field illumination. The UV (360–370 nm) and Vis (520–550 nm) beams emitted from the objective were employed to maintain the *cis*/*trans* states for the isomerization reaction. In the case of "$Y_{2x1x5}$ (*cis*)" with $T_D$ of approximately 3°C, some ice blocks were placed near the sample to maintain the surrounding temperature below 10°C.

6. Measurement of the MSD and signed diffusion coefficient $D^*$

**Trajectory detection** The time-series data of the photogenerated migrations recorded by the IX71 (frame interval of 200 ms and exposure of 100 ms) were subjected to particle tracking analysis using TrackMate[57], an open-source plugin in Fiji. We chose the LoG detector for the particle detection and the Simple LAP tracker for the particle linker in the parameter settings (Supplementary Fig. 3). Therefore, to maximize the duration of detected paths, the track filter was adjusted to select the tracks spanning the entire recording time.

**MSD** We calculated the MSDs of individual trajectories in each experiment, including tens to hundreds of the detected trajectories, from the two-dimensional trajectories acquired above. Additionally, to reasonably reduce the computational cost for large calculations, we referred to a useful algorithm that yields MSDs through Fast Fourier Transform[65]. Its underlying idea is to use the Wiener–Khinchin theorem, which relates the power spectrum of a given signal with its auto-correlated function via the Fourier transform. To focus on the significant MSD curves, the obtained MSD curves as a function of time interval $\tau$ were reduced to the first 20% of the entire time data points. Up to 20 MSD plots with the steepest curves were sorted out in each plot for the representative demonstration of the MSDs (Fig. 6c,d).

***D** plot** Linear curve fitting was applied against the last 20% data points in each MSD plot to obtain the unsigned diffusion coefficient $D'$ (Fig. 6a), and we determined $D'$ from the fitted slope of $4D'$ (Supplementary eq. 2). Subsequently, up to 20 MSD curves with the largest $D'$ values were sorted out in each case to obtain signed $D^*$ in Fig. 6b. Finally, the direction of the generated migrations was determined qualitatively. Four experiments were included ($n = 4$) at each temperature examined.

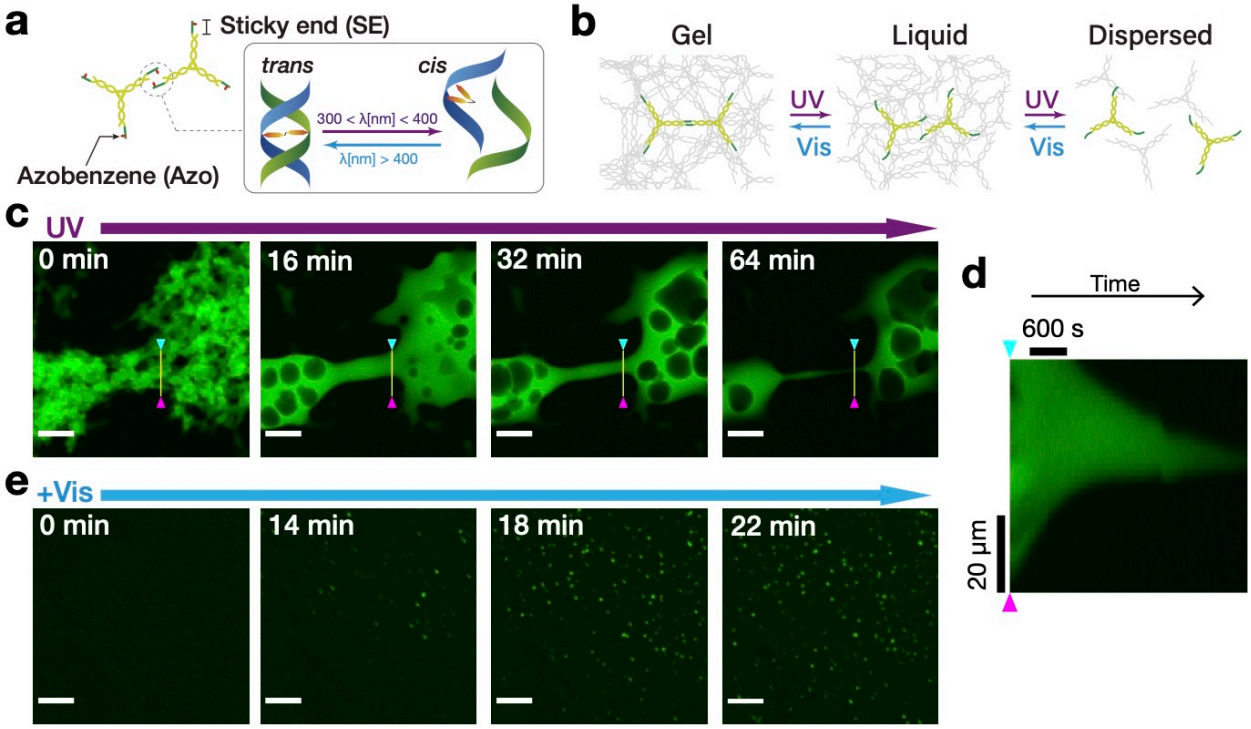


**Fig. 1 Fluidity regulation using the photocontrolled state transition of DNA fluid.** Schematics of **a** Y-shaped nanostructures of DNA (Y-motifs) with azobenzene (Azo) inserted in the sticky ends (SEs) and **b** photoswitchable state transition of DNA fluid. **c**, Representative time-lapse imaging using confocal microscopy of UV-induced gel-to-liquid state transition of DNA fluid (Supplementary Table 3) at 56°C. At the yellow lines, **d** a kymograph is yielded for the whole time series capturing the pinching-off and rounding-up of the liquefied DNA fluid. **e**, Time-lapse imaging of Vis-induced dispersed-to-liquid/gel state transition at 56°C. DNA was stained with SYBR Gold (green). Scale bars (**c**, **e**), 50 $\mu$m.

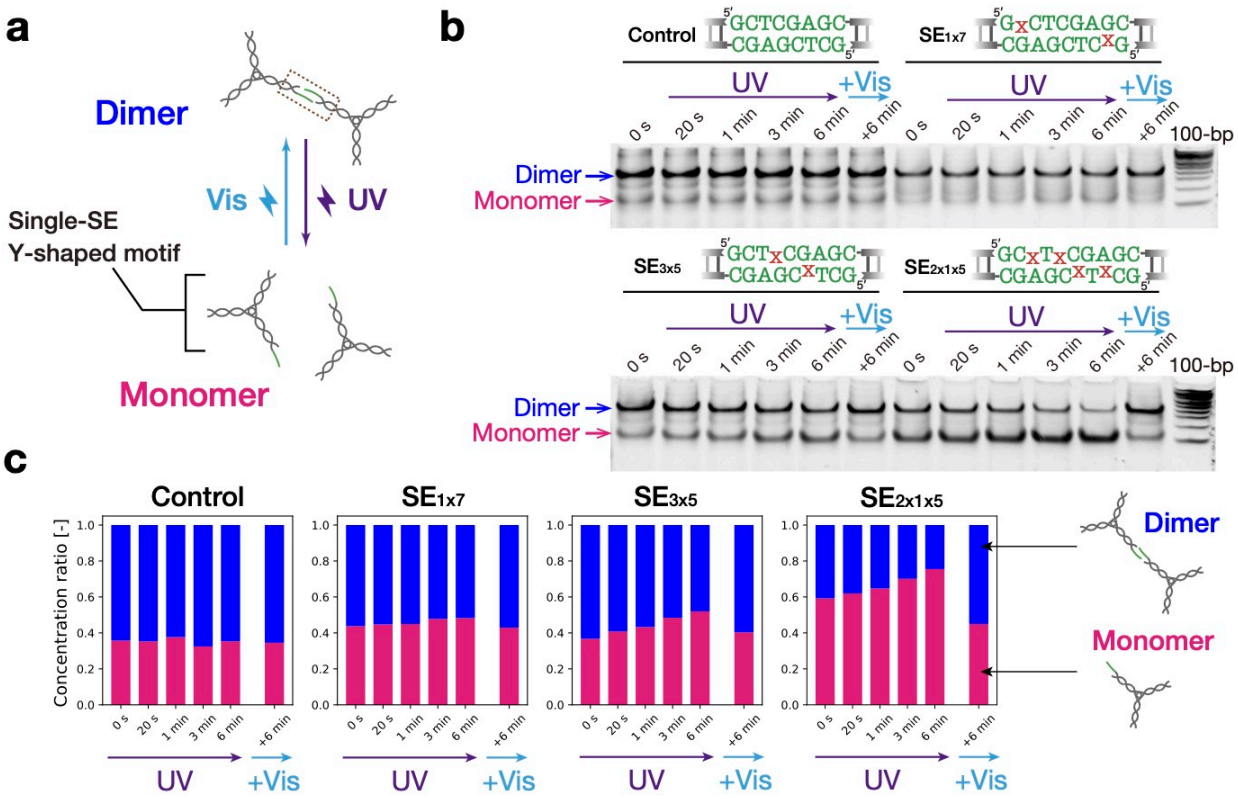


**Fig. 2 Proof of concept for photoswitchable state transition. a**, Y-motifs with a single SE were used to generate binary bands in native polyacrylamide gel electrophoresis (PAGE). The upper and lower bands correspond to the dimer and monomer states, respectively. **b**, PAGE results. Lane labels refer to time durations of UV (0–6 min) and additional Vis (+6 min) irradiation. "100-bp" means 100-bp (base pair) DNA ladder. (Top) Illustration of 8-bp hybridized SE sequences marked within the dashed-line box in **a**. "x" denotes an inserted Azo. **c**, Bar plots for the concentrations of dimers and monomers measured from the band intensities in **b**. The intensity values in each lane are normalized by the total integrated intensity.

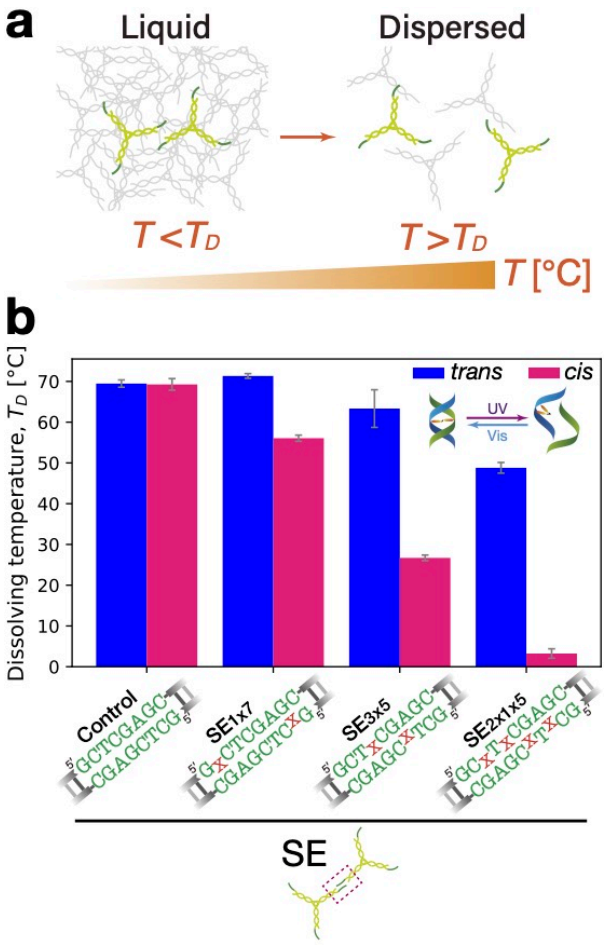


**Fig. 3 Experimental evaluation of SEs' binding strength. a**, Dissolving temperature $T_D$ as a quantifiable indicator of the binding strength. Above $T_D$, DNA fluid becomes dispersed with increasing temperature $T$. **b**, Bar plots of $T_D$ as a function of the insertion site of Azo in the SE. Error bars, S.D. ($n = 3$). Note that for "Control," the blue and magenta bars refer to the Vis and UV irradiation instead of *trans* and *cis*, respectively.

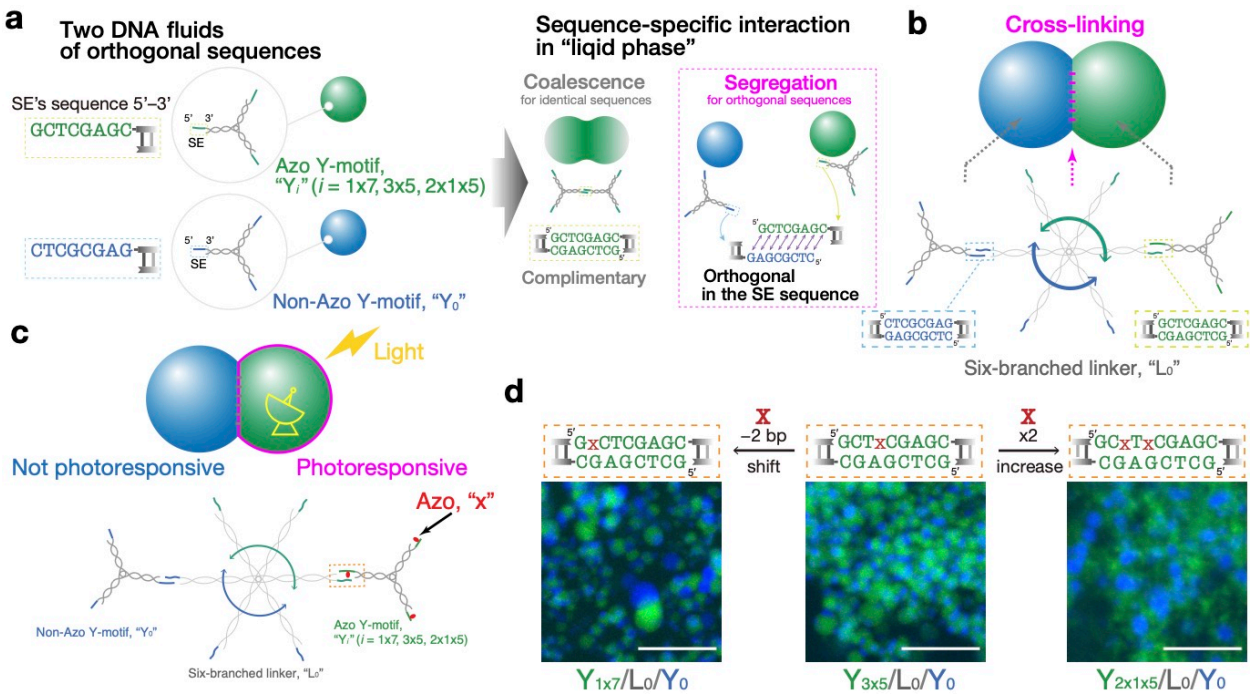


**Fig. 4 Sequence-specific photoresponsive capability using sequence programmability. a**, Sequence-specific selectivity in fluid interaction. Due to the palindromic sequence in the SE, DNA fluids in a liquid state (DNA liquids) with the same sequence favor coalescence; DNA liquids with orthogonal sequences in the SE favor segregation. **b**, A six-branched cross-linker that binds with both Y-motifs form an adhered structure of the two immiscible DNA fluids. **c**, DNA fluid achieves sequence-specific photoresponsive capability by introducing Azo in one of the cross-linked orthogonal motifs. Photoresponsive DNA fluid with the SE bearing Azo ($SE_i$) is referred to as $Y_i$ ($i$ = 1x7, 3x5, 2x1x5); DNA fluid without Azo as $Y_0$; and the six-branched cross-linker as $L_0$. Three neighboring SEs (blue and green) in $L_0$ exclusively hybridize with $Y_0$ and $Y_i$ motifs, respectively. $Y_0$ motif was double-labeled with Alexa Fluor 405 and Cy3 for the observation under UV irradiation (360–370 nm; for *trans*-to-*cis* experiments) and Vis (520–550 nm; for *cis*-to-trans experiments), respectively. $Y_i$ motifs were labeled with FAM for Vis (460–495 nm) irradiation. **d**, (Top) Illustration of the hybridized SEs between $L_0$ and $Y_i$, marked in the dashed-line box in **c**. (Bottom) Merged confocal microscopy images for adhered structures of immiscible DNA fluids in a gel state (*trans*) at room temperature (RT). Below each image, $Y_i/L_0/Y_0$ denotes the corresponding cross-linked DNA motifs containing $Y_i$ ($i$ = 1x7, 3x5, 2x1x5, green, FAM). Scale bars, 20 $\mu$m.

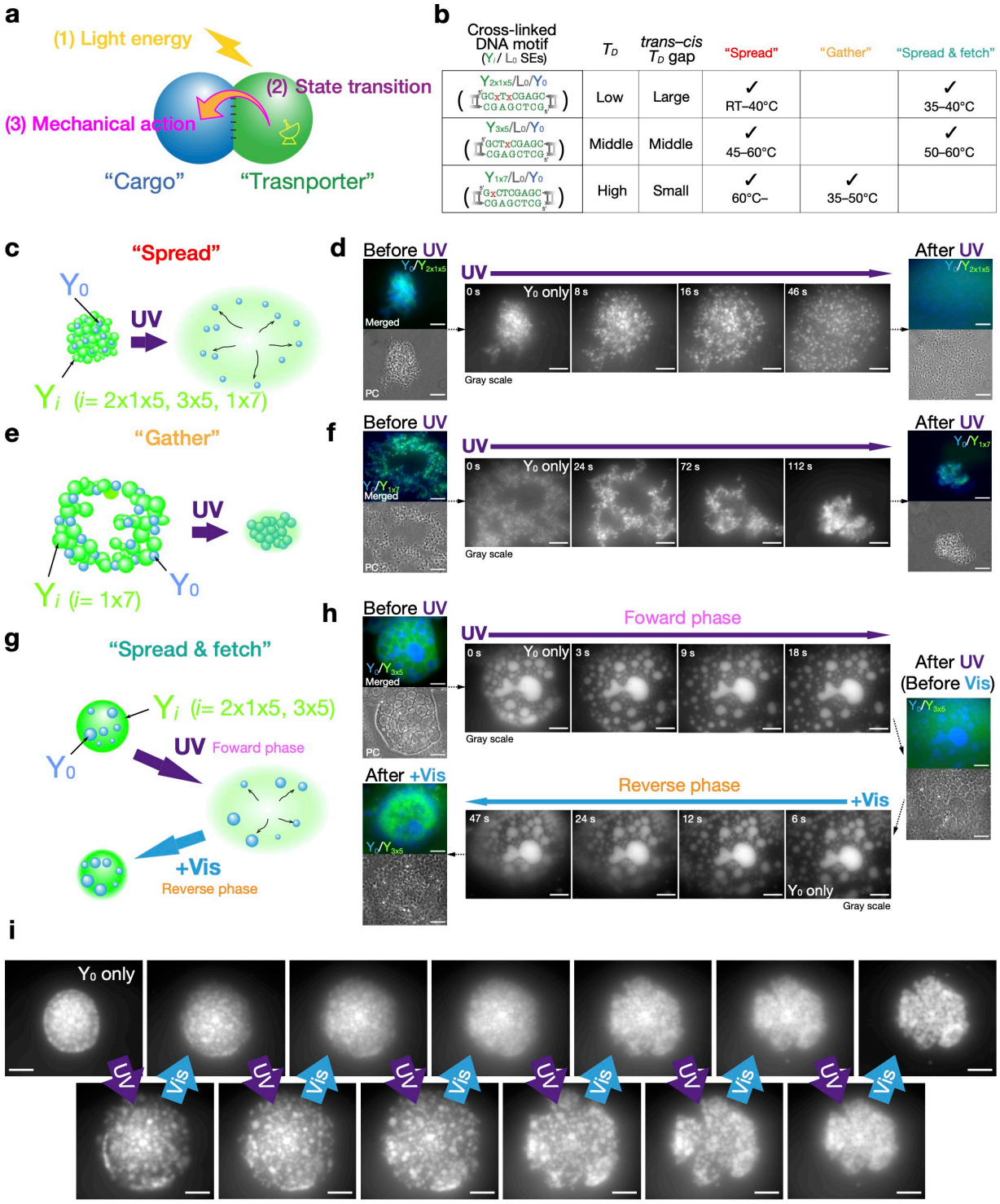


**Fig. 5 Mechanical actions using microflow of DNA fluid. a**, Schematic of an energy-transducing system that performs a microfluidic mechanical action of state-transitioning transporter' DNA acting on "cargo" DNA. Sequence-specific programming of photoresponsiveness enables differentiated roles in this action. **b**, Summary table of generated flow modes (**c**, **e**, **g**) and their

observed temperature ranges for different insertion sites of Azo in the SE. Dissolving temperature $T_D$ for the corresponding SEs (Fig. 3) are also related. **c**, **d** "Spread" mode due to UV-induced fast diffusion. **c**, Upon UV irradiation, "transporter" DNA ($Y_i$) favors a fast gel-to-dispersed state transition, leading to the fast spread of "cargo" DNA ($Y_0$) in the outward direction. $i$ = 2x1x5, 3x5, 1x7. **d** (Top) Merged fluorescence and (bottom) phase-contrast (PC) images for $Y_{2x1x5}/L_0/Y_0$ captured (leftmost) before and (rightmost) after UV irradiation at 30°C. (Middle) Time-evolution fluorescence images of the "spreading" of $Y_0$ particles in response to UV irradiation. **e**, **f** "Gather" mode due to UV-induced gel-to-liquid state transition. **e**, Upon UV irradiation, "transporter" ($Y_i$) shows a gel-to-liquid state transition; as a result of the emerging surface tension effect, "cargo" ($Y_0$) gel particles are subjected to drastic compaction. $i$ = 1x7. **f**, Merged fluorescence and PC images for $Y_{1x7}/L_0/Y_0$ captured (leftmost) before and (rightmost) after UV irradiation at 45°C. (Middle) Time-evolution fluorescence images of the "gathering" of $Y_0$ particles in response to UV irradiation. **g**, **h** "Spread and fetch" in alternating UV/Vis irradiation. **g**, Initially, "transporter" ($Y_i$) and "cargo" ($Y_0$) are in a liquid state and coexist in a droplet. Upon UV irradiation, $Y_i$ liquid shows "spread" behavior due to liquid-to-dispersed state transition and releases $Y_0$ liquid; upon switching to Vis irradiation, dispersed $Y_i$ liquid shows reversing flow due to Vis-induced reassociation of SEs and subsequent increased entropic elasticity, and fetches the released $Y_0$ liquid. **h**, Merged fluorescence and PC images for $Y_{3x5}/L_0/Y_0$ captured (top leftmost) before UV, (rightmost) after UV, and (bottom leftmost) after additional Vis irradiation at 55°C. Time-evolution fluorescence images of (top middle, left-to-right) the "spreading" of $Y_0$ liquid droplets under UV irradiation and (bottom, right-to-left) "fetching" of $Y_0$ droplets after switching to Vis. **i**, Macroscopic reversibility in "spread and fetch" mode of $Y_{3x5}/L_0/Y_0$ fluid under alternating UV/Vis irradiation at 55°C. Each image was captured at each filter exchange. Scale bars, 50 $\mu$m.

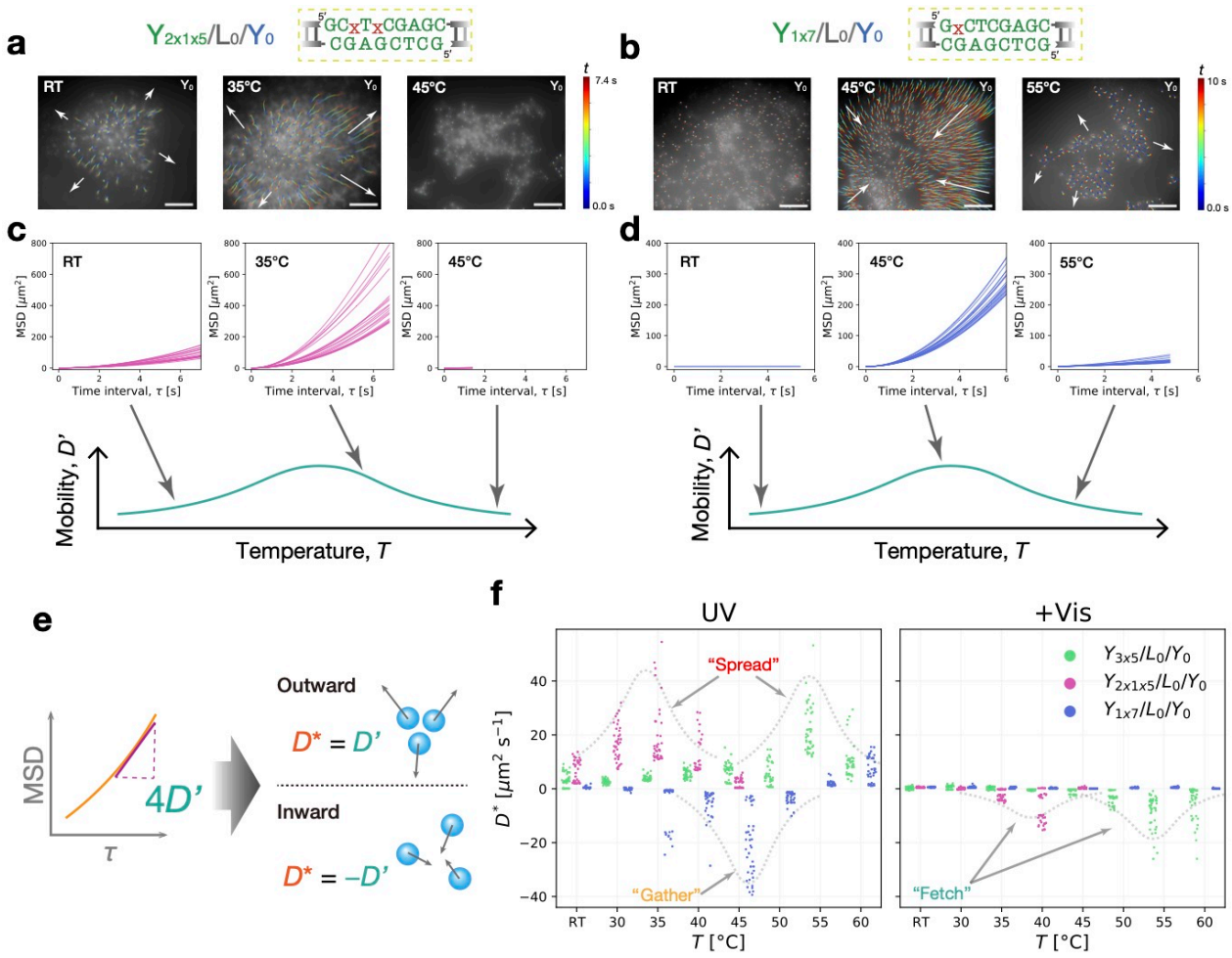


**Fig. 6 Reentrant flow mobility of mode-switchable photoinduced microflow of DNA fluid.** **a–d**, Each flow mode possessed the lowest mobility in high- and low-temperature ranges and the highest flow mobility in the middle-temperature range. Particle tracking of "cargo" ($Y_0$) DNA particles for **a** "spread" mode of $Y_{2x1x5}/L_0/Y_0$ and for **b** "gather" mode of $Y_{1x7}/L_0/Y_0$. Detected trajectory paths are visualized in a color map of an elapsed time $t$ [s]. Arrows indicate the flow directions. Representative plots of calculated mean square displacements (MSDs) as a function of time interval $\tau$ for the **c** "spread" mode (from **a)** and for the **d** "gather" mode (from **b)**. Low, middle, and high-temperature ranges were sampled. **e**, Unsigned diffusion coefficient $D'$ and signed diffusion coefficient $D^*$, arbitrarily defined to allow for the direction of flow. The diffusion coefficient $D'$ expressing the mobility of individual migration paths was calculated by taking the linear curve fitting against a calculated MSD curve. The signed diffusion coefficient $D^*$ was then determined by adding a positive or negative sign to $D'$ depending on the direction of the generated flow. **f**, Plots of signed $D^*$ as a function of temperature $T$ in UV and following Vis

irradiation. Data points of $Y_i/L_0/Y_0$ ($i$ = 1x7, 3x5) are staggered sideways for ease of recognition at each temperature examined.

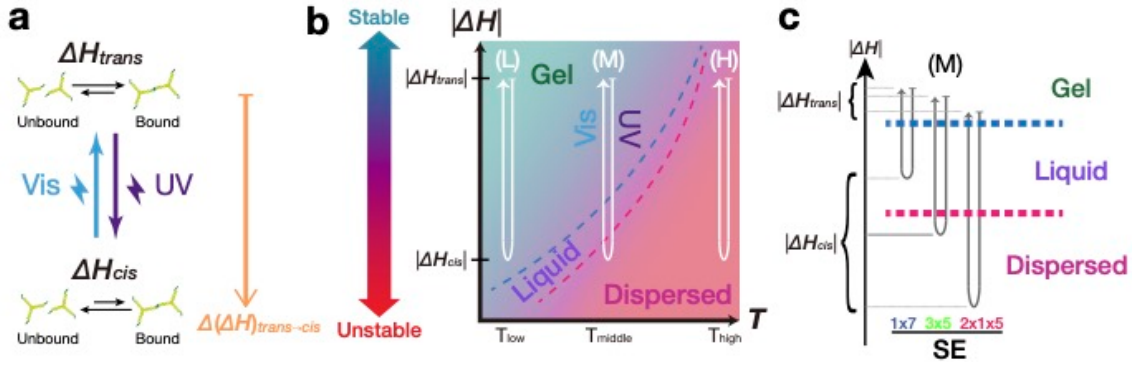


**Fig. 7 Dynamic enthalpy fine-tuning of DNA fluid as an underlying mechanism of mode-switchable reentrant flow behavior**. **a**, Schematic of the enthalpy difference between the bound and unbound states of two motifs $\Delta H$, which varies according to the isomer of the inserted Azo residues. UV irradiation generates a shift in $\Delta H$ by an amount of $\Delta(\Delta H)_{trans\rightarrow cis} = \Delta H_{cis} - \Delta H_{trans}$. **b**, Phase diagram that spans the $|\Delta H|$-$T$ space. $|\Delta H|$ corresponds to the binding strength of SEs. Isomerization pathways of SEs for UV irradiation are added in (L) low, (M) middle, and (H) high temperature ranges. **c**, Insertion site of Azo in the SE determines the magnitude of a dynamic enthalpy shift $|\Delta(\Delta H)_{trans\rightarrow cis}|$, and a specific flow mode is favored.

**REFERENCES < 70 items**


1. Sato, Y., Hiratsuka, Y., Kawamata, I., Murata, S. & Nomura, S. M. Micrometer-sized molecular robot changes its shape in response to signal molecules. *Sci. Robot.* **2**, (2017).

2. Dobson, J. Remote control of cellular behaviour with magnetic nanoparticles. *Nat. Nanotechnol.* **3**, 139–143 (2008).

3. Lee, K., Yi, Y. & Yu, Y. Remote Control of T Cell Activation Using Magnetic Janus Particles. *Angew. Chemie Int. Ed.* **55**, 7384–7387 (2016).

4. Chen, C.-C. *et al*. DNA–Gold Nanorod Conjugates for Remote Control of Localized Gene Expression by near Infrared Irradiation. *J. Am. Chem. Soc.* **128**, 3709–3715 (2006).

5. Mittasch, M. *et al*. Non-invasive perturbations of intracellular flow reveal physical principles of cell organization. *Nat. Cell Biol.* **20**, 344–351 (2018).

6. Zhang, Y. *et al*. Giant Coacervate Vesicles As an Integrated Approach to Cytomimetic Modeling. *J. Am. Chem. Soc.* **143**, 2866–2874 (2021).

7. Hann, S. Y., Cui, H., Nowicki, M. & Zhang, L. G. 4D printing soft robotics for biomedical applications. *Addit. Manuf.* **36**, 101567 (2020).

8. Linsenmeier, M. *et al*. Dynamics of Synthetic Membraneless Organelles in Microfluidic Droplets. *Angew. Chemie Int. Ed.* **58**, 14489–14494 (2019).

9. Bico, J., Reyssat, É. & Roman, B. Elastocapillarity: When Surface Tension Deforms Elastic Solids. *Annu. Rev. Fluid Mech.* **50**, 629–659 (2018).

10. Agudo-Canalejo, J. *et al*. Wetting regulates autophagy of phase-separated compartments and the cytosol. *Nature* **591**, 142–146 (2021).

11. Schulman, R. D. *et al*. Elastocapillary bending of microfibers around liquid droplets. *Soft Matter* **13**, 720–724 (2017).

12. Masukawa, M. K., Okuda, Y. & Takinoue, M. Aqueous Triple-Phase System in Microwell Array for Generating Uniform-Sized DNA Hydrogel Particles. *Front. Genet.* **12**, 1–11 (2021).

13. Lee, C.-Y., Chang, C.-L., Wang, Y.-N. & Fu, L.-M. Microfluidic Mixing: A Review. *Int. J. Mol. Sci.* **12**, 3263–3287 (2011).

14. Shang, L., Cheng, Y. & Zhao, Y. Emerging Droplet Microfluidics. *Chem. Rev.* **117**, 7964–8040 (2017).

15. Yamada, M. & Seki, M. Microfluidic particle sorter employing flow splitting and recombining. *Anal. Chem.* **78**, 1357–1362 (2006).

16. Ichimura, K., Oh, S.-K. & Nakagawa, M. Light-Driven Motion of Liquids on a Photoresponsive Surface. *Science (80-. ).* **288**, 1624–1626 (2000).

17. Berná, J. *et al*. Macroscopic transport by synthetic molecular machines. *Nat. Mater.* **4**, 704–710 (2005).

18. Brangwynne, C. P. *et al*. Germline P Granules Are Liquid Droplets That Localize by Controlled Dissolution/Condensation. *Science (80-. ).* **324**, 1729–1732 (2009).

19. Shin, Y. & Brangwynne, C. P. Liquid phase condensation in cell physiology and disease. *Science (80-. ).* **357**, eaaf4382 (2017).

20. Handwerger, K. E. & Gall, J. G. Subnuclear organelles: New insights into form and function. *Trends Cell Biol.* **16**, 19–26 (2006).

21. Weber, S. C. & Brangwynne, C. P. Inverse Size Scaling of the Nucleolus by a Concentration-Dependent Phase Transition. *Curr. Biol.* **25**, 641–646 (2015).

22. Nott, T. J., Craggs, T. D. & Baldwin, A. J. Membraneless organelles can melt nucleic acid duplexes and act as biomolecular filters. *Nat. Chem.* **8**, 569–575 (2016).

23. Li, P. *et al*. Phase transitions in the assembly of multivalent signalling proteins. *Nature* **483**, 336–340 (2012).

24. Feric, M. *et al*. Coexisting Liquid Phases Underlie Nucleolar Subcompartments. *Cell* **165**, 1686–1697 (2016).

25. Strickfaden, H. *et al*. Condensed Chromatin Behaves like a Solid on the Mesoscale In Vitro and in Living Cells. *Cell* **183**, 1772-1784.e13 (2020).

26. Patel, A. *et al*. A Liquid-to-Solid Phase Transition of the ALS Protein FUS Accelerated by Disease Mutation. *Cell* **162**, 1066–1077 (2015).

27. Kool, E. T. Preorganization of DNA: Design Principles for Improving Nucleic Acid Recognition by Synthetic Oligonucleotides. *Chem. Rev.* **97**, 1473–1488 (1997).

28. Seeman, N. C. DNA in a material world. *Nature* **421**, 427–431 (2003).

29. Seeman, N. C. & Sleiman, H. F. DNA nanotechnology. *Nat. Rev. Mater.* **3**, 17068 (2018).

30. Winfree, E., Liu, F., Wenzler, L. A. & Seeman, N. C. Design and self-assembly of two-dimensional DNA crystals. *Nature* **394**, 539–544 (1998).

31. Ishikawa, D. *et al*. DNA Origami Nanoplate-Based Emulsion with Nanopore Function. *Angew. Chemie Int. Ed.* **58**, 15299–15303 (2019).

32. Um, S. H. *et al*. Enzyme-catalysed assembly of DNA hydrogel. *Nat. Mater.* **5**, 797–801 (2006).

33. Li, J. *et al*. Functional nucleic acid-based hydrogels for bioanalytical and biomedical applications. *Chem. Soc. Rev.* **45**, 1410–1431 (2016).

34. Sato, Y., Sakamoto, T. & Takinoue, M. Sequence-based engineering of dynamic functions of micrometer-sized DNA droplets. *Sci. Adv.* **6**, eaba3471 (2020).

35. Merindol, R., Loescher, S., Samanta, A. & Walther, A. Pathway-controlled formation of mesostructured all-DNA colloids and superstructures. *Nat. Nanotechnol.* **13**, 730–738 (2018).

36. Saleh, O. A., Jeon, B. J. & Liedl, T. Enzymatic degradation of liquid droplets of DNA is modulated near the phase boundary. *Proc. Natl. Acad. Sci. U. S. A.* **117**, 16160–16166 (2020).

37. Sato, Y. & Takinoue, M. Capsule-like DNA Hydrogels with Patterns Formed by Lateral Phase Separation of DNA Nanostructures. *JACS Au* **2**, 159–168 (2022).

38. Jeon, B. *et al*. Salt-dependent properties of a coacervate-like, self-assembled DNA liquid. *Soft Matter* **14**, 7009–7015 (2018).

39. Jeon, B., Nguyen, D. T. & Saleh, O. A. Sequence-Controlled Adhesion and Microemulsification in a Two-Phase System of DNA Liquid Droplets. *J. Phys. Chem. B* **124**, 8888–8895 (2020).

40. Samanta, A., Sabatino, V., Ward, T. R. & Walther, A. Functional and morphological adaptation in DNA protocells via signal processing prompted by artificial metalloenzymes. *Nat. Nanotechnol.* **15**, 914–921 (2020).

41. Bomboi, F. *et al*. Re-entrant DNA gels. *Nat. Commun.* **7**, 13191 (2016).

42. Palagi, S. *et al*. Structured light enables biomimetic swimming and versatile locomotion of photoresponsive soft microrobots. *Nat. Mater.* **15**, 647–653 (2016).

43. Ikeuchi, N. *et al*. Light-Regulated Liquid–Liquid Phase Separation for Spatiotemporal Protein Recruitment and Cell Aggregation. *ACS Appl. Mater. Interfaces* **13**, 5652–5659 (2021).

44. Asanuma, H. *et al*. Synthesis of azobenzene-tethered DNA for reversible photo-regulation of DNA functions: hybridization and transcription. *Nat. Protoc.* **2**, 203–212 (2007).

45. Hidaka, T., Wee, W. A., Yum, J. H., Sugiyama, H. & Park, S. Photo-Controllable Phase Transition of Arylazopyrazole-Conjugated Oligonucleotides. *Bioconjug. Chem.* **32**, 2129–2133 (2021).

46. Le Ny, A.-L. M. & Lee, C. T. Photoreversible DNA Condensation Using Light-Responsive Surfactants. *J. Am. Chem. Soc.* **128**, 6400–6408 (2006).

47. Kandatsu, D. *et al*. Reversible Gel-Sol Transition of a Photo-Responsive DNA Gel. *ChemBioChem* **17**, 1118–1121 (2016).

48. Wee, W. A., Sugiyama, H. & Park, S. Photoswitchable single-stranded DNA-peptide coacervate formation as a dynamic system for reaction control. *iScience* **24**, 103455 (2021).

49. Martin, N. *et al*. Photoswitchable Phase Separation and Oligonucleotide Trafficking in DNA Coacervate Microdroplets. *Angew. Chemie Int. Ed.* **58**, 14594–14598 (2019).

50. Rogers, W. B. & Manoharan, V. N. Programming colloidal phase transitions with DNA strand displacement. *Science (80-. ).* **347**, 639–642 (2015).

51. Angioletti-Uberti, S., Mognetti, B. M. & Frenkel, D. Re-entrant melting as a design principle for DNA-coated colloids. *Nat. Mater.* **11**, 518–522 (2012).

52. Asanuma, H. *et al*. Enantioselective Incorporation of Azobenzenes into Oligodeoxyribonucleotide for Effective Photoregulation of Duplex Formation. *Angew. Chemie Int. Ed.* **40**, 2671–2673 (2001).

53. Griffiths, J. II. Photochemistry of azobenzene and its derivatives. *Chem. Soc. Rev.* **1**, 481 (1972).

54. Fischer, E., Frankel, M. & Wolovsky, R. Wavelength dependence of photoisomerization equilibria in azocompounds. *J. Chem. Phys.* **23**, 1367 (1955).

55. Beharry, A. A. & Woolley, G. A. Azobenzene photoswitches for biomolecules. *Chem. Soc. Rev.* **40**, 4422 (2011).

56. Nishimura, N. *et al*. Thermal Cis -to- Trans Isomerization of Substituted Azobenzenes II. Substituent and Solvent Effects. *Bull. Chem. Soc. Jpn.* **49**, 1381–1387 (1976).

57. Tinevez, J.-Y. *et al*. TrackMate: An open and extensible platform for single-particle tracking. *Methods* **115**, 80–90 (2017).

58. Howse, J. R. *et al*. Self-Motile Colloidal Particles: From Directed Propulsion to Random Walk. *Phys. Rev. Lett.* **99**, 048102 (2007).

59. Dunderdale, G., Ebbens, S., Fairclough, P. & Howse, J. Importance of particle tracking and calculating the mean-squared displacement in distinguishing nanopropulsion from other processes. *Langmuir* **28**, 10997–11006 (2012).

60. Asanuma, H., Matsunaga, D. & Komiyama, M. Clear-cut photo-regulation of the formation and dissociation of the DNA duplex by modified oligonucleotide involving multiple azobenzenes. *Nucleic Acids Symp. Ser.* **49**, 35–36 (2005).

61. Dias, A. R. *et al*. Enthalpies of formation of cis-azobenzene and trans-azobenzene. *J. Chem. Thermodyn.* **24**, 439–447 (1992).

62. Hernandez-Verdun, D. Assembly and disassembly of the nucleolus during the cell cycle. *Nucleus* **2**, 189–194 (2011).

63. Weber, S. C. Sequence-encoded material properties dictate the structure and function of nuclear bodies. *Curr. Opin. Cell Biol.* **46**, 62–71 (2017).

64. Paxton, W. F. *et al*. Catalytically Induced Electrokinetics for Motors and Micropumps. *J. Am. Chem. Soc*. **128**, 14881–14888 (2006).

65. Calandrini, V., Pellegrini, E., Calligari, P., Hinsen, K. & Kneller, G. R. nMoldyn - Interfacing spectroscopic experiments, molecular dynamics simulations and models for time correlation functions. *École thématique la Société Française la Neutron*. **12**, 201–232 (2011).

**Acknowledgements**

We thank Dr. Marcos K. Masukawa and Dr. Yu Fujio (Tokyo Institute of Technology), Prof. Yusuke Sato (Kyushu Institute of Technology), Prof. Hirohide Saito (Kyoto University), and Prof. Yoshihiro Shimizu (RIKEN) for instructive discussion and suggestions. We also appreciate useful experimental tip instructions by Ms Yukiko Okuda, Ms Jing Gong, and Mr Tomoya Maruyama (Tokyo Institute of Technology). This work was supported by MEXT/JSPS KAKENHI (No. JP20H05701 to S.M.N. and M.T., Nos. JP20H00619 and JP20H05935 to M.T., No. JP22K14528 to H.U.) and JSPS Grant-in-Aid for JSPS fellows (Nos. JP19J112959 and JP22J00940 to H.U).

**Author contributions**

H.U., S.M.N., and M. T. contributed equally to the conceptualization and the research design. H.U. conducted experiments and data analysis, and wrote the first draft of the manuscript. H.U., S.M.N., and M.T. revised the manuscript.

**Competing interests**

The authors declare no conflict of interest.

**Data availability**

All observational data and Python codes for the data analysis are reasonably requested from M.T.